

# CrystEngComm

Accepted Manuscript



This is an *Accepted Manuscript*, which has been through the Royal Society of Chemistry peer review process and has been accepted for publication.

*Accepted Manuscripts* are published online shortly after acceptance, before technical editing, formatting and proof reading. Using this free service, authors can make their results available to the community, in citable form, before we publish the edited article. We will replace this *Accepted Manuscript* with the edited and formatted *Advance Article* as soon as it is available.

You can find more information about *Accepted Manuscripts* in the [Information for Authors](#).

Please note that technical editing may introduce minor changes to the text and/or graphics, which may alter content. The journal's standard [Terms & Conditions](#) and the [Ethical guidelines](#) still apply. In no event shall the Royal Society of Chemistry be held responsible for any errors or omissions in this *Accepted Manuscript* or any consequences arising from the use of any information it contains.

## ARTICLE

# Role of synthesis variables on controlled nucleation and growth of hexagonal molybdenum oxide nanocrystals: Investigation on thermal and optical properties

Cite this: DOI: 10.1039/x0xx00000x

Received 00th January 2012,  
Accepted 00th January 2012

DOI: 10.1039/x0xx00000x

www.rsc.org/

A. Chithambararaj<sup>a</sup> and A. Chandra Bose<sup>a,\*</sup>

Solution based chemical precipitation route has been utilized for the controlled synthesis of novel and single phase three dimensional (3D) hierarchical flower-like microspheres of hexagonal molybdenum oxide (h-MoO<sub>3</sub>) nanocrystals. The nucleation, formation and the growth mechanism of h-MoO<sub>3</sub> nanocrystals were examined as a function of synthesis variables such as the type of chemical oxidant, oxidant concentration, solvent medium, reaction time and reaction temperature. The growth mechanism was proposed and it involves four main consecutive stages: (1) homogeneous nucleation of h-MoO<sub>3</sub> via dissociation and association of precursors at a controlled reactant species, reactant concentration and solvent medium and (2) self-assembly process for the formation anisotropic growth of hexagonal phase MoO<sub>3</sub> nuclei (3) evaluation of 1D hexagonal rods through Ostwald ripening and (4) formation of 3D hierarchical flower-like microspheres via interparticle interaction with the assistance of reaction time and temperature. Among the various synthesis variables, the relative ratio of the oxidant to the chemical precursor (HNO<sub>3</sub> / AHM) and the nature of the solvent medium greatly influence the formation of h-MoO<sub>3</sub> nanocrystals with a controlled morphology and reduced crystallite size. The results were supported with crystal phase analysis by X-ray diffraction (XRD), functional analysis by Fourier transform infrared spectroscopy (FT-IR), morphology and particle size analysis by scanning electron (SEM) and transmission electron microscopy (TEM). Further, the samples were characterized by thermogravimetric analysis (TGA) and diffuse reflectance spectroscopy (DRS) to analyze the thermal and optical properties. The results showed that the optical absorption of h-MoO<sub>3</sub> nanocrystals were strongly dependent on the size and crystallinity. The as-synthesized h-MoO<sub>3</sub> displayed an excellent visible light absorption. In addition, the reasons behind the bandgap tuning obtained under varying synthesis conditions were also discussed.

## Introduction

The self-assembly of hierarchical inorganic 3D nano/micro architectures such as flowers, spheres, octahedron, snowflake, fishbone and others with precisely controlled crystal structure, size, shape and surface functionalities have been receiving considerable attention due to their enhanced physical and chemical properties that are in demand forever. Over the past two decades, synthesis of hierarchical architectures, especially through solution based chemical routes has been acknowledged for their capabilities to produce a variety of metals, semiconductors, and metal oxide nanocrystals. Because, the solution based synthesis route provides a soft chemical approach where, the preparations are often carried out at low temperatures (below 250 °C) with the precise control of nucleation and particle growth. This offers a control over homogeneity, develop high purity and meta-stable phase

materials with narrow size distribution and large scale production of anisotropic architectural building blocks. Moreover, the dimensional control of a material in nanoscale regime can be well achieved by the systematic and careful regulation of thermodynamic parameters and growth kinetics in liquid media under the assistance of selected solvents, ligands, surfactants or catalyst additives.<sup>1-9</sup> Among the various inorganic solids, MoO<sub>3</sub> is of great technological importance due to its structure, size and shape dependent material properties and possesses potential applications in optoelectronics, catalysis, Li-ion batteries, electrochromics, photocatalysis, storage devices, and sensors. The crystalline MoO<sub>3</sub> has three polymorphs: thermodynamically stable orthorhombic  $\alpha$ -MoO<sub>3</sub> phase, two meta-stable phases such as monoclinic ( $\beta$ -MoO<sub>3</sub>) and hexagonal (h-MoO<sub>3</sub>). Currently, the research is focused on the meta-stable h-MoO<sub>3</sub>, as they exhibit unique and enhanced

material properties compared to the stable structure.<sup>10-14</sup> Our recent research findings proved that the phase selectivity of h-MoO<sub>3</sub> resulted in the photocatalytic activity with 6 to 8 folds higher than the other phase structure of MoO<sub>3</sub>. Such a unique properties in h-MoO<sub>3</sub> attributed to the one dimensional (1D) structure, tunnel behaviour and defect free band structure.<sup>15, 16</sup> Although, MoO<sub>3</sub> nanocrystals of different phases and shapes have been successfully synthesized through various soft chemical synthesis routes, reporting an optimal experimental condition for well-developed crystal structure, size, and shape including the nucleation and growth mechanism is still lacking. In particular, the systematic control of the synthesis variables, such as choice and the relative concentrations of oxidant, solvent, reaction time and reaction temperature on the preparation of h-MoO<sub>3</sub> have not been reported.

Thus, the present investigation motivates towards the controlled synthesis of 3D hierarchical flower-like h-MoO<sub>3</sub> through solution based chemical precipitation route. In order to understand the process of nucleation and particle growth, the influence of various synthesis variables on the controlled morphology and size tuning was examined systematically. The formation of h-MoO<sub>3</sub> was well supported by different characterization techniques including XRD, FT-IR, SEM, and TEM. In addition, the thermal and optical properties were elucidated by TGA and DRS measurements.

## Experimental Procedure

### Chemicals

Ammonium hepta-molybdate (AHM), concentric nitric acid (HNO<sub>3</sub>), hydrochloric acid (HCl), deionized water (H<sub>2</sub>O), ethanol and heptane were purchased and the reagents were used without further purification. The h-MoO<sub>3</sub> was prepared by dissolving 2.43 g of AHM in 10 mL of deionized water. The relative ratio of AHM / HNO<sub>3</sub> concentration was varied by adding 3 mL, 5 mL, 10 mL and 15 mL of HNO<sub>3</sub> while AHM concentration was kept constant as 0.2 M. The reactant mixture was heated at 85 °C for 60 min and the precipitates were collected by centrifugation. The powders were finally washed several times with water and ethanol, and then dried in vacuum oven at 70 °C for 6 h. To optimize the synthesis condition and to establish a control on the morphology, the synthesis variables (type of chemical oxidant, oxidant concentration, solvent medium, reaction time and reaction temperature) were tuned effectively as tabulated in the Table 1.

### Instrumentation

The crystal structure of the powder was determined with Ultima III Rigaku X-ray diffractometer at a scanning rate of 0.2°/min in the range of 5°-60° with Cu K<sub>α1</sub> radiation (1.5406 Å) operated at 40 kV and 35 mA. The morphological study was carried out with field emission SEM (FESEM, Hitachi S-4800 and S-3000) operated at an accelerating voltage 5-10 kV and transmission electron microscopy (TEM, JEOL JEM FXII 2000) operated at an accelerating voltage of 100 kV. FT-IR spectra were recorded by Perkin Elmer, Spectrum RX1 spectrometer in the range of 4000-400 cm<sup>-1</sup> using KBr as the reference. The differential thermal analysis (DTA) / differential thermal gravimetric (DTG) and thermogravimetric analysis (TGA) were studied using EXSTAR6200 thermal analyzer and the measurement was carried out in nitrogen atmosphere at a heating rate of 10 °C/min from room temperature to 550 °C. UV-Vis DRS measurement was acquired using T90+ UV/Vis spectrophotometer. BaSO<sub>4</sub> powder was used as reference and

the spectrum was recorded at room temperature in the wavelength range of 300 nm - 700 nm with the speed of 0.5 nm/s.

## Results

The influence of each synthesis variables on the formation of 3D hierarchical flower-like microspheres of h-MoO<sub>3</sub> nanocrystals were carried out and elaborated below.

### Role of oxidant and oxidant concentration

In chemical precipitation, the choice and the concentration of reactant oxidant decides the nucleation and growth rate of h-MoO<sub>3</sub> nanocrystals. Thus, initially the role of oxidant and oxidant concentration was studied using HNO<sub>3</sub> and HCl as an oxidant and the concentrations were varied as 3 mL, 5 mL, 10 mL and 15 mL. Fig. 1 shows the XRD patterns of MoO<sub>3</sub> samples synthesized with varying concentrations of HNO<sub>3</sub>.

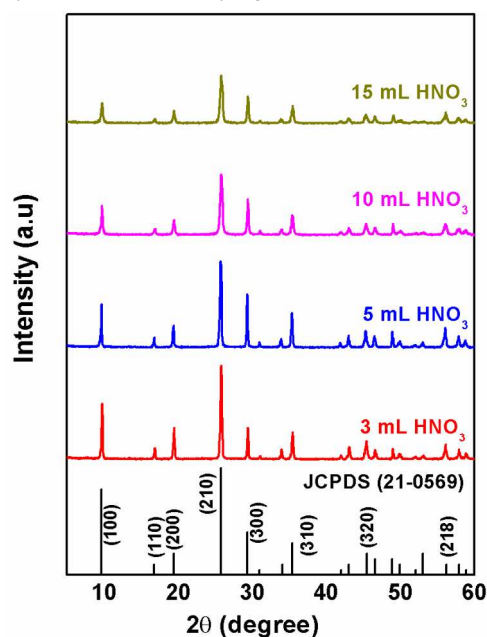


**Fig. 1** XRD pattern of as-synthesized h-MoO<sub>3</sub> samples prepared with different HNO<sub>3</sub> concentrations

All the samples exhibit a diffraction pattern corresponding to the hexagonal phase MoO<sub>3</sub> with reference to the standard JCPDS data card no. 21-0569. Thus, the samples crystallize in single phase without any secondary impurity phase. All the peaks in XRD pattern revealed that the synthesized samples were polycrystalline nature. The high intense peak at 26°, indexed as (210) plane represents the preferred growth direction of h-MoO<sub>3</sub> samples. The phase remains the same even with the increase in HNO<sub>3</sub> concentration from 3 mL to 15 mL. However, the peak intensity, peak broadening and peak shift in the XRD varies with respect to HNO<sub>3</sub> concentration. With the increase in HNO<sub>3</sub> concentration, the peak broadening increases (ref. Fig. S1(a)) and the intensity of the peak decreases (ref. Fig. S1(b)) implying that the synthesized samples were poor crystalline with reduced crystallite size. The peak shift with respect to high intense peak indexed as (210) plane was plotted in Fig. S1(a) and the observed peak shift in the samples attributed to the presence of the strain evolved during the synthesis. From the plot, it can be inferred that the 5 mL concentration of HNO<sub>3</sub> to be the better oxidant concentration. Here, the (210) plane of the

synthesized sample matches well with the standard sample revealing the good crystallinity of the sample. The crystallite size ( $D_{hkl}$ ) and strain ( $\epsilon_{hkl}$ ) variation in the as-synthesized h-MoO<sub>3</sub> were estimated by Scherrer's ( $D_{hkl} = k\lambda/\beta_{hkl}\cos\theta_{hkl}$ , where  $\lambda$  is the wavelength of  $CuK_{\alpha 1}$  radiation (1.5406 Å),  $\theta_{hkl}$  is the Bragg diffraction angle and ( $hkl$ ) are Miller indices of the concerned lattice planes) and Stokes-Wilson ( $\epsilon_{hkl} = \beta_{hkl}/4\tan\theta_{hkl}$ ) methods<sup>17</sup> and the values are summarized in Table 1. The result demonstrates that the crystallite size of h-MoO<sub>3</sub> gradually reduced with increase in HNO<sub>3</sub> concentration, and the calculated strain values were in micron range. Thus, the resultant broadening in the diffraction peaks were mainly due to the reduced crystallite size of h-MoO<sub>3</sub>.

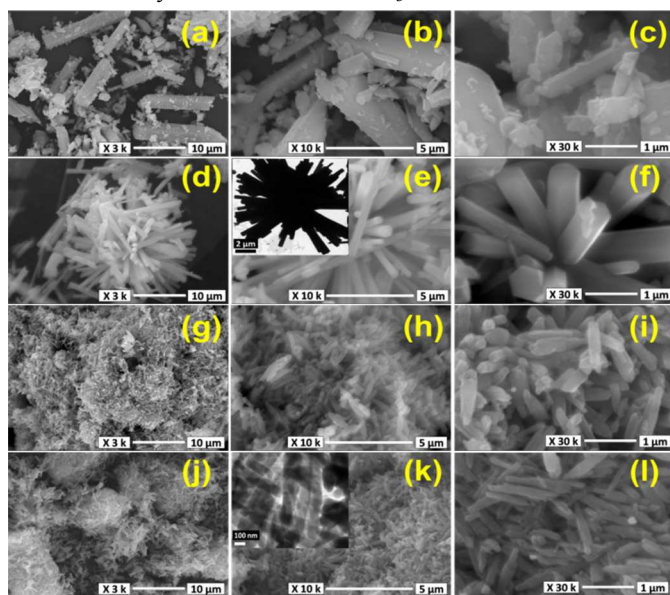


**Fig. 2** Low and high magnified SEM images of as-synthesized h-MoO<sub>3</sub> samples prepared with different HNO<sub>3</sub> concentrations: (a-c) 3 mL; (d-f) 5 mL; (g-i) 10 mL and (j-l) 15 mL; TEM images of h-MoO<sub>3</sub> samples prepared with 5 mL HNO<sub>3</sub> (inset e) and 15 mL HNO<sub>3</sub> (inset k) concentrations

Further, the observed inference from the XRD was supported by the SEM and TEM images displayed in Fig. 2. The Fig. (a-c) displays the SEM images of h-MoO<sub>3</sub> nanocrystals synthesized with 3 mL concentration of HNO<sub>3</sub>. Here, the sample was composed of agglomerated micro rods and larger sized particles. This composition mixture reveals the incomplete nucleation of the sample product. However, well-defined 3D hierarchical flower-like microspheres of h-MoO<sub>3</sub> were obtained with increase in the HNO<sub>3</sub> concentration as 5 mL (ref. Fig. 2(d-f)). The rods were distinct and have a hexagonal face with smooth and even surface. The average length and diameter of the hexagonal rods were decreased and the rods were self-oriented to form flower-like microspheres with an average diameter of 2 μm to 3 μm. The high magnified TEM image shown as an inset in Fig. 2e clearly depicts that these microspheres were an aggregation of long microrods which were emanating from the centers. The typical diameter and the length of the rods were around 300 nm to 350 nm and 1.2 μm to 1.5 μm, respectively. With the further increase in HNO<sub>3</sub> concentration to 10 mL (ref. Fig. 2(g-i)) and 15 mL (ref. Fig. 2(j-l)), the flower-like architecture disappeared and resulted in an irregular morphology with reduced particle size. The inset of Fig. 2k represents the TEM image of the as-synthesized sample

with 15 mL concentration of HNO<sub>3</sub>. It clearly depicts that the rods were highly aggregated and randomly oriented.

The functional groups presented in the h-MoO<sub>3</sub> were analyzed using FT-IR spectroscopy and are represented in Fig. S2. The IR peaks indicate the presence of OH<sup>-</sup> (3480 cm<sup>-1</sup> and 1622 cm<sup>-1</sup>) and NH<sub>4</sub><sup>+</sup> group (3184 cm<sup>-1</sup> and 1403 cm<sup>-1</sup>) in h-MoO<sub>3</sub>. The metal-oxygen characteristic bands of h-MoO<sub>3</sub> were identified in the range of 1000 cm<sup>-1</sup> - 400 cm<sup>-1</sup>.<sup>18</sup> A keen observation of FT-IR results suggest that the h-MoO<sub>3</sub> synthesized from 5 mL HNO<sub>3</sub> concentration shows sharp and well distinct vibrational peaks attributed to the high degree of order and periodicity of MoO<sub>3</sub> species with less surface defects. However, the samples obtained from other concentrations (3 mL, 10 mL and 15 mL) show broad and undefined absorption peaks often associated with a non-uniform behavior of Mo-O co-ordinations, structural defects and/or dangling bonds at the surface. To analyze the significance of the oxidant, the second oxidant namely HCl was utilized and the same experimental studies were performed and compared. Fig. S3(a) shows the XRD diffraction patterns of the samples synthesized with different concentrations of HCl. All the patterns show identical diffraction peaks which exactly match with the single phase h-MoO<sub>3</sub>. The result clearly concludes that the choice of oxidant does not bring a change in the crystal phase of the material. However, in controversy with the HNO<sub>3</sub> condition, the poor crystallinity (peak intensity variation) and large crystallite size (peak broadening analysis) were observed and were anomalously varied with respect to HCl concentrations (ref. Table 1 and Fig. S3(b)). As specific inference was drawn from XRD, the samples were further characterized by SEM (ref. Fig. S4(a-h)). The entire samples synthesized with varying concentration of HCl (3 mL to 15 mL) shows hexagonal rod like morphology. The length of the rods was in the micron range. The rods were distributed very randomly and were not aligned regularly to define a unique morphology. This paves the way towards the synthesis of 3D hierarchical flower-like microspheres of h-MoO<sub>3</sub> nanocrystals in the presence of HNO<sub>3</sub> with a particular concentration.

#### Role of solvent (water: ethanol: heptane)

To gain insight into the role of solvents on the crystallite size, morphology and surface chemistry, three different solvents such as water, ethanol and heptane were employed. The precise control over the volume ratio of water/ethanol and water/heptane were carried out, in order to know the chemistry of the varying polar groups and the coordination nature on the controlled morphology. Fig. S5 and Fig. S6 shows the XRD patterns of MoO<sub>3</sub> nanocrystals synthesized under varying water/ethanol and water/heptane ratios, respectively. All the peaks were indexed and assigned to h-MoO<sub>3</sub>. With the varying concentration of ethanol or heptane concentration, the phase remains unaltered, while the intensity and broadening of the diffraction peak varies significantly. The diffraction peak significantly increases with ethanol concentration whereas it diminished with the rise in heptane concentration and this was assigned to a resultant of poor crystallinity of the samples. The average crystallite size was calculated from the peak broadening analysis. The crystallite size was increased from 46 nm to 56 nm with increase in ethanol concentration (ref. Table 1) while it decreased gradually from 46 nm to 24 nm with increase in heptane concentration (ref. Fig. S5(b) and S6(b)).

This may bring changes in the morphology of the as-synthesized samples, which were examined by SEM and TEM micrographs. Figs. 3 and 4 show the SEM and TEM images of samples synthesized using water, ethanol and heptane as a

reactant solvent. Well-defined, even and monodispersed hexagonal rods were obtained when water was used as a solvent medium (ref. SEM image in Fig. 3(a-b) and TEM image in Fig. 4(a-b)).

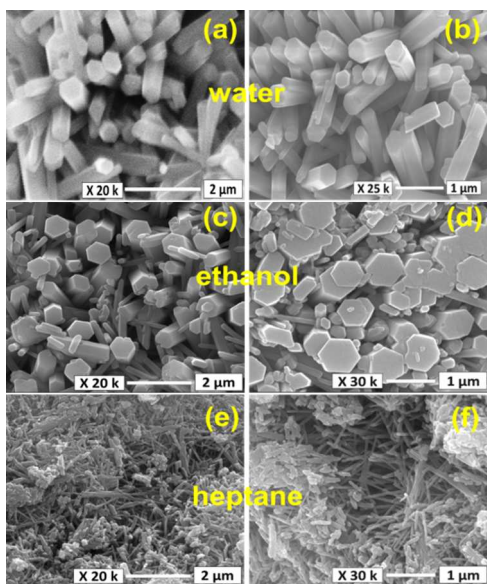


**Fig. 3** Low and high magnified SEM images of as-synthesized h-MoO<sub>3</sub> samples synthesized using water (a and b), ethanol (c and d) and heptane (e and f)

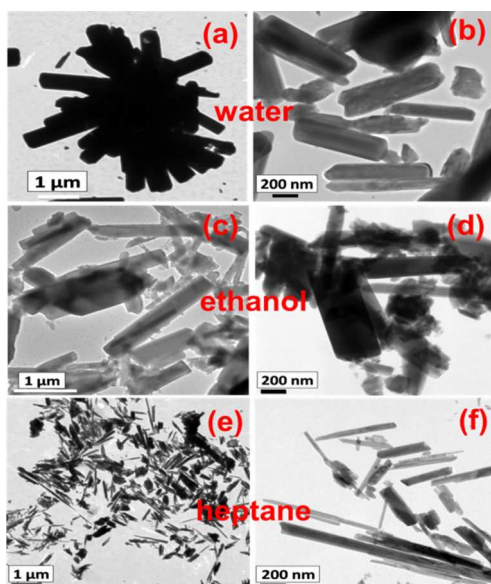


**Fig. 4** Low and high magnified TEM images of as-synthesized h-MoO<sub>3</sub> samples synthesized using water (a and b), ethanol (c and d) and heptane (e and f)

On the other hand, when ethanol was used, 1D hexagonal rods were obtained but with a wide particle size distribution ranging from 100 nm to 700 nm (ref. Fig. 3(c-d)). The TEM image showed in Fig 4(c-d) indicates the presence of both short and long rods. In the case of heptane, 1D nanorods were formed with thin diameter and large aspect ratio. Moreover, the rods showed non-hexagonal geometry. They were highly dense and agglomerated and were mixed up with particles thus, resulting in non-uniform dispersibility (ref. SEM image in Fig. 3(e-f) and

TEM image in Fig. 4(e-f)). Moreover, the mixed solvent compositions (water/ethanol and water/heptane) favor asymmetrical chemical environment resulting in non-uniform and distorted hexagonal rods as shown in Fig. S7 and S8. From the morphological study, one can conclude that the water act as a suitable solvent medium in rendering dissolution and homogeneity of the reactant molecules. These features promote the formation of 1D hexagonal shape as well as 3D hierarchical flower-like morphology in h-MoO<sub>3</sub> nanocrystals.

### Role of reaction time and temperature

The reaction time and the reaction temperature are the other significant factors influencing the chemical reaction pathway, nucleation and growth of the resultant products. The time and temperature dependent experiments were carried out by varying the reaction time from 30 min to 180 min and temperature varied as 120 °C, 150 °C and 180 °C. Under the above synthesis conditions, the oxidant concentration (HNO<sub>3</sub>) and the reactant solvent (water) were placed constant. Fig. S9(a) shows the XRD patterns of the samples synthesized at varying reaction time and temperature. In general, the rise in the reaction time and the reaction temperature allow the crystallite to nucleate, grow along a specific growth sites, and arrange orderly, thus, promote high crystalline samples with increased crystallite size. The saying well agreed with the XRD pattern shown in Fig. S9(a). Here, the phase remains unaltered and the diffraction peak intensity increases with reaction time and temperature. Thus, the reaction time and reaction temperature can tune the average crystallite size from 40 nm to 52 nm (ref. Fig. S9(b) and Table 1). Fig. 5(a-i) shows the SEM images of h-MoO<sub>3</sub> obtained at 120 °C for 60 min, 120 min and 180 min reaction time. The samples synthesized at a lower reaction time (60 min (ref. Fig. 5(a-c)) and 120 min (ref. Fig. 5(d-f))), show particles of non-uniform size distribution and most of the rods are having irregular morphology.

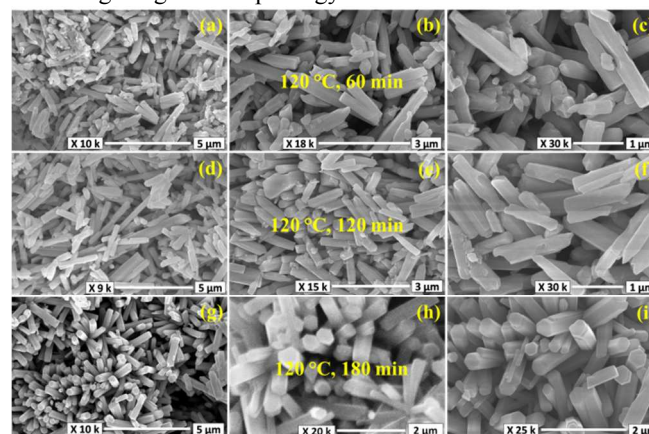


**Fig. 5** Low and high magnified SEM images of the h-MoO<sub>3</sub> samples obtained at 120 °C for different reaction time: (a-c) 60 min; (d-f) 120 min and (g-i) 180 min

But, increasing the reaction time to 180 min, the hexagonal rods have a tendency to grow in size and the irregular hexagonal rods gradually turned to regular morphology. In Fig. 5(g-i), the sample composed of fairly monodispersed and highly oriented attachment of hierarchical flower-like microspheres of h-MoO<sub>3</sub>. It is interesting to note that when the reaction temperature was raised to 150 °C and 180 °C, well-developed flower-like structures were observed for lower reaction time at 60 min and 30 min, respectively as shown in Fig. 6(a-c) and 7(a-c). The 3D

flower-like architectures grew even faster by increasing the reaction temperature, thus affecting the uniform morphology and crystalline quality of the products. However, on further extending the reaction time at higher temperatures (for 150 °C - 120 min and 180 min and for 180 °C - 60 min and 90 min), the hierarchical flower-like microspheres were gradually dissolved and re-aggregated into broken particles with rugged morphology (ref. Fig. 6(d-i) and ref. Fig. 7(d-i)).

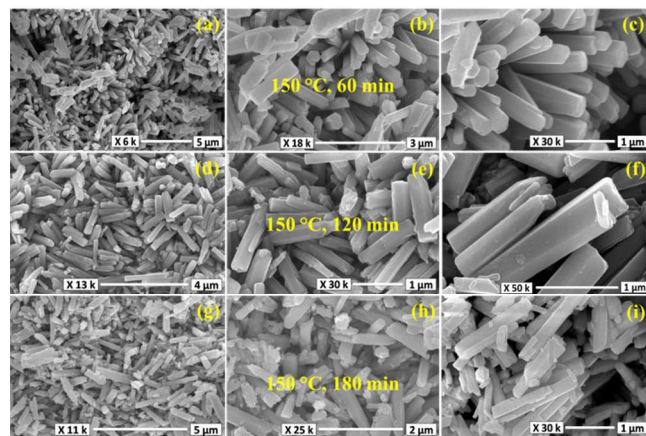


**Fig. 6** Low and high magnified SEM images of the h-MoO<sub>3</sub> samples obtained at 150 °C for different reaction time: (a-c) 60 min; (d-f) 120 min and (g-i) 180 min

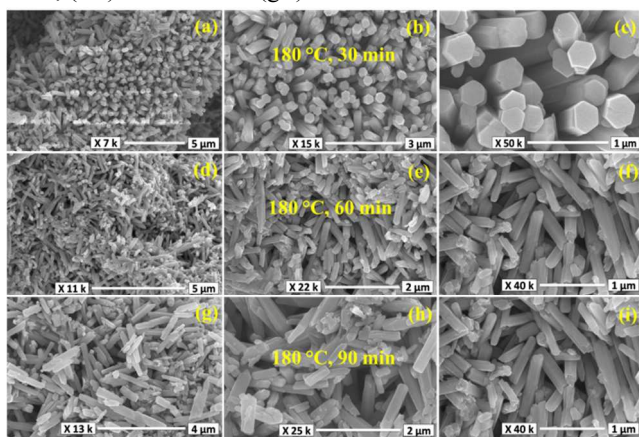


**Fig. 7** Low and high magnified SEM images of the h-MoO<sub>3</sub> samples obtained at 180 °C for different reaction time: (a-c) 30 min; (d-f) 60 min and (g-i) 90 min

From the experimental results, it was concluded that the lower reaction temperature with longer reaction time or higher reaction temperature with short reaction time develop well-defined crystal morphology. On the contrary, other conditions, the weakened interactions between the molecules and the increased degree of distortion results in broken rods and induces non-uniform morphology of the particles. All these investigations conclude that there is a specific time and temperature required to reach well-defined morphology of the particles.

## Discussion

### Formation mechanism of hierarchical flower-like microspheres of h-MoO<sub>3</sub> nanocrystals

On the basis of experimental conditions and characterization results, it was found that oxidant, oxidant concentration, solvent medium, reaction temperature and time play an important role

in the formation of 3D hierarchical flower-like microspheres of h-MoO<sub>3</sub> nanocrystals. A possible stepwise formation mechanism is proposed and schematically depicted in Fig. 8 to Fig. 12.

The formation mechanism of hierarchical flower-like microstructures of h-MoO<sub>3</sub> nanocrystals can be mainly divided into four main consecutive stages: (1) homogeneous nucleation of h-MoO<sub>3</sub> via dissociation and association of precursors at a controlled reactant species, reactant concentration and solvent medium and (2) self-assembly process for the formation anisotropic growth of hexagonal phase MoO<sub>3</sub> nuclei (3) evaluation of 1D hexagonal rods through Ostwald ripening and (4) formation of 3D hierarchical flower-like microspheres via interparticle interaction with the assistance of reaction time and temperature.

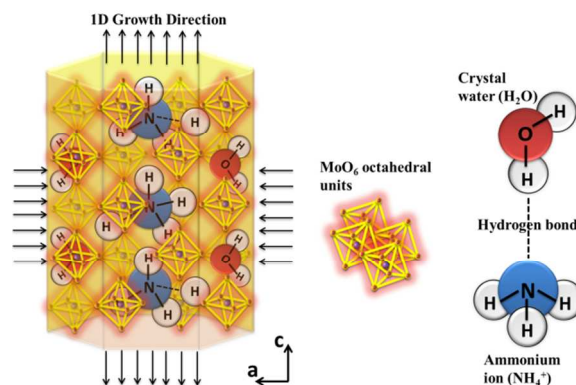
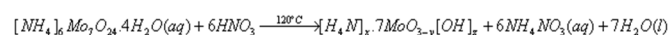


**Fig. 8** The schematic representation of the formation mechanism of 1D hexagonal rods of h-MoO<sub>3</sub>

The chemical reaction was initiated by the dissociation and association of reactant precursor molecules ammonium heptamolybdate tetrahydrate (AHM) and nitric acid (HNO<sub>3</sub>) in the water solvent medium. The reaction leads to the ionization of molecules to form a variety of hydrolyzed ion species, such as Mo<sub>7</sub>O<sub>24</sub><sup>+</sup>, NH<sub>4</sub><sup>+</sup>, OH<sup>-</sup>, H<sup>+</sup> and NO<sub>3</sub><sup>-</sup> ions. As the reaction time extended, the ionized species within the reaction medium reaches its solubility limit and attains supersaturation.<sup>19, 20</sup> The dissociation and association of these ionized species favor the formation of MoO<sub>6</sub> octahedral crystal nuclei known as the basic building unit of MoO<sub>3</sub> where the molybdenum is located at the center and octahedrally coordinated to six oxygen atoms as illustrated in Fig. 8. Thus, by continuous nucleation, solidification and growth, the crystallites were precipitated in the reaction solution. Under this condition, the as formed MoO<sub>6</sub> octahedral crystal unit subsequently rotate, coalesce and self-integrate with the assistance of ammonium (NH<sub>4</sub><sup>+</sup>) along the c-direction (corner sharing), and with crystal water (H<sub>2</sub>O) along the a-direction (edge sharing) through charge neutralization and oriented attachment, thus, resulting an anisotropic growth of hexagonal phase MoO<sub>3</sub> nuclei as represented schematically in Fig. 8. Thus, at an optimum reaction temperature and reaction time, the precursors were gradually consumed and favored liquid-solid transformation. Further, the h-MoO<sub>3</sub> nuclei strongly integrate via Ostwald ripening processes with the newly formed h-MoO<sub>3</sub> nuclei, thus tend to develop larger sized 1D hexagonal rods. Finally, the grown larger rods in different directions interconnected themselves by interparticle interactions via any one of the following interactions such as electrostatic/dipolar interactions, van der Waals interaction, hydrophobic interactions or hydrogen bonds and thus emerges hierarchical

flower-like 3D microspheres.<sup>15, 21</sup> The possible chemical reactions may occur synchronously or asynchronously as follows:



With this proposed growth mechanism, the influences of each synthesis conditions were elaborated sequentially.

### Chemical oxidant and oxidant concentration

In our experimental work, chemical oxidants HNO<sub>3</sub> and HCl were utilized for the synthesis of h-MoO<sub>3</sub>. These two oxidants differ in their ionic strength, coordination environment and the interactions of their anions (NO<sub>3</sub><sup>-</sup> and Cl<sup>-</sup>) with the precursors. The above differences brought change in the dissociation and association process as well as in the reaction affinity and the reaction chemical potential which were all responsible for controlling the crystallite size and final distribution of the particles (incomplete and distorted h-MoO<sub>3</sub> in HCl assisted samples and well-developed h-MoO<sub>3</sub> microspheres for HNO<sub>3</sub> condition). From the results, HNO<sub>3</sub> is found to be a suitable oxidant and thus providing an optimized reaction environment for the synthesis of hierarchical flower-like microspheres of h-MoO<sub>3</sub> as depicted in Fig. 9.

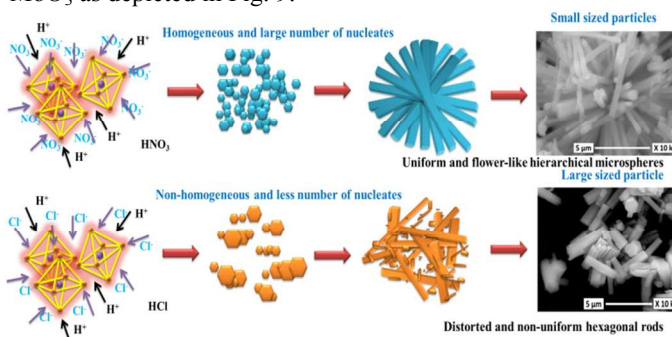


**Fig. 9** The schematic representation of the role of oxidant on the nucleation and growth of h-MoO<sub>3</sub> nanocrystals

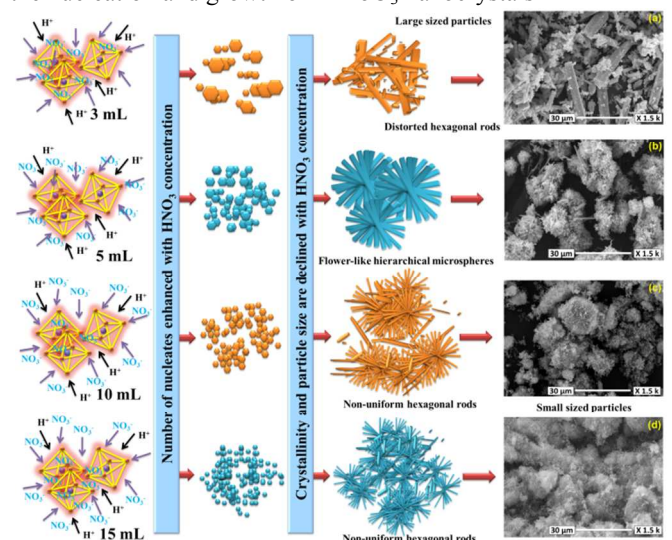


**Fig. 10** The schematic representation of the role of oxidant concentration (a) 3 mL; (b) 5 mL; (c) 10 mL and (d) 15 mL of HNO<sub>3</sub> on the nucleation and growth of h-MoO<sub>3</sub> nanocrystals

Further, the influence of HNO<sub>3</sub> concentration on the synthesis of h-MoO<sub>3</sub> is explained as follows: in the case of low HNO<sub>3</sub>

concentration, the limited surface coverage fraction of nucleophilic H<sup>+</sup> and NO<sub>3</sub><sup>-</sup> ions between the reactants (MoO<sub>6</sub>, OH<sup>-</sup> and NH<sub>4</sub><sup>+</sup>) provides insufficient reactant's collision, ionic diffusion and migration. The above incomplete processes that affect the interfacial tension, mass transfer and condensation rate that promotes faster nucleation and growth rate resulting in larger particle size and irregular morphology<sup>22</sup> as clearly demonstrate in Fig. 10(a-d). Whereas, increasing HNO<sub>3</sub> concentrations, increased surface coverage fraction of H<sup>+</sup> ion and NO<sub>3</sub><sup>-</sup> ion binds strongly to the nucleates and provide sufficient time for collision and diffusion of the ions at the crystal surfaces which offers steric shielding for the nucleation as well as the growth of the particles. This effect enables the nuclei to nucleate at a higher rate and slow growth rate, resulting in reduced crystallite size with a high agglomeration of particles.<sup>23</sup> With the above discussion, the 5 mL concentration of HNO<sub>3</sub> was considered to be the better condition in favoring the controlled dissolution and solidification for the growth of h-MoO<sub>3</sub> nanocrystals in well-defined morphology.

### Solvent

The role of solvent on the resultant crystallite size (51 nm for ethanol, 46 nm for water and 24 nm for heptane) and the morphology (1D hexagonal rod for ethanol and water; 1D non-hexagonal rods for heptane) is explained by the difference in polarity (ethanol-polar solvent, water-neutral solvent and heptane-non-polar solvent), dielectric constant, boiling point, viscosity and density of solvents. This affected the binding affinity, coordination nature, electrostatic interaction within the reactant constituents, surface tension, and diffusivity thus defining the solubility and supersaturation. Thus, the above said factors are significantly changing the nucleation rate as well as the surface free energy at the different facets of the particles and resulting changes in crystallite size and final morphology of h-MoO<sub>3</sub>.<sup>24</sup> In our case, the observed hexagonal shape of crystals for water (monodispersed hexagonal rods) and ethanol (polydispersed hexagonal rods) is mainly due to the presence of OH<sup>-</sup> ions in the reaction system. The OH<sup>-</sup> ions in the system greatly affect the surface free energy of particles as well as enhance the hydrolysis reaction and dissolution-crystallization process prompting much faster growth resulting in larger particle size with a hexagonal cross section.

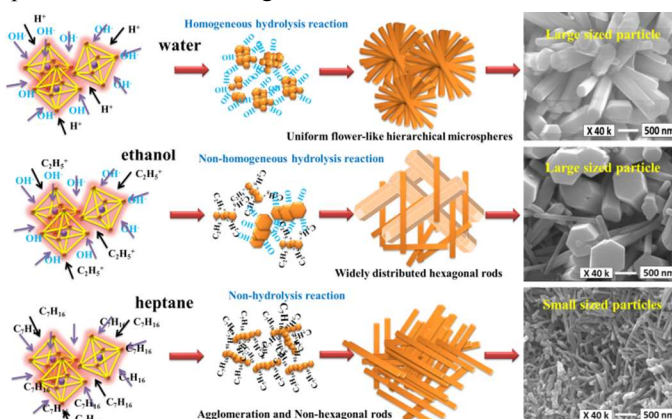


**Fig. 11** The schematic representation of the role of solvent medium on the nucleation and growth of h-MoO<sub>3</sub> nanocrystals

In addition, the competition between H<sup>+</sup> and C<sub>2</sub>H<sub>5</sub><sup>+</sup> adsorption on h-MoO<sub>3</sub> nucleates (MoO<sub>6</sub>/OH/H<sup>+</sup> and MoO<sub>6</sub>/OH/C<sub>2</sub>H<sub>5</sub><sup>+</sup>)

which thought to play an important role in the particle distribution. Whereas, the non-hexagonal shape and the resultant of reduced particle size for heptane system is assigned to the non-surface related reactions ( $\text{MoO}_6/\text{C}_7\text{H}_{16}$ ) and non-hydrolysis reaction results change in surface free energy and slowing down the dissolution-crystallization process as well as mass transport limitations as illustrated in Fig. 11.<sup>25</sup> On the basis of the above experimental evidence, water is proven to be a better solvent for the synthesis of monodispersed and hierarchical flower-like  $\text{h-MoO}_3$  nanocrystals.

### Reaction time and temperature

Finally, the time (kinetic) and temperature (thermodynamic) dependent study reveals the complete growth mechanism of  $\text{h-MoO}_3$  nanocrystals. Until a particular reaction time and temperature, the growth mechanism is proposed as an Ostwald ripening process for the growth of nanoparticles to 1D micro rods and the interparticle interactions for the design of 3D hierarchical flower-like microspheres. At a particular temperature, the precursors are gradually consumed with respect to time and strongly integrate via Ostwald ripening processes with the newly formed  $\text{h-MoO}_3$  nuclei thus tend to develop larger sized 1D hexagonal rods and obviously stop at final particle size (ref. conditions 120 °C for 60 min and 120 min).

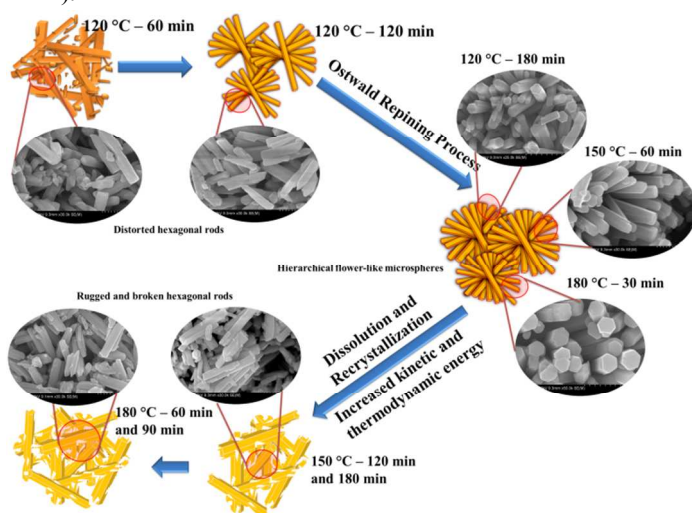


**Fig. 12** The schematic representation of the role of reaction time and temperature on the growth of  $\text{h-MoO}_3$  nanocrystals

Further extending the reaction time to 180 min, hierarchical flower-like 3D microspheres were developed by interparticle interactions as depicted in Fig. 12. As expected, increase in the reaction temperature leads to a faster dissolution of intermediate results in well-developed architectures emerged at short reaction time (ref. conditions 150 °C for 60 min and 180 °C for 30 min). However, on further extending the reaction time or temperature, the particle surfaces was destroyed and have a tendency to dissolve the particles. This results in breaking up the balance between individual rods suggesting a surface dissolution and surface re-crystallization process takes place as shown in conditions for 150 °C for 120 min and 180 min and 180 °C for 60 min and 90 min (ref. Fig. 12). This is mainly due to the increased kinetic and thermodynamic energy which introduces larger residual stresses that favors an asymmetrical chemical environment in the reaction system.<sup>26</sup> Thus, it is concluded that appropriate reaction temperature and time

provides sufficient energy input to promote the reactants speed and strong attractive interactions resulted in controlled nucleation and growth towards a well-developed hierarchical flower-like  $\text{h-MoO}_3$  microstructures.

### Thermal properties

To quantify the thermal properties and the phase stability, the samples synthesized at different reaction conditions (120 °C for 3h, 150 °C for 1h and 180 °C for 30 min) were characterized with TGA processed under nitrogen atmosphere as shown in Figs. 13.

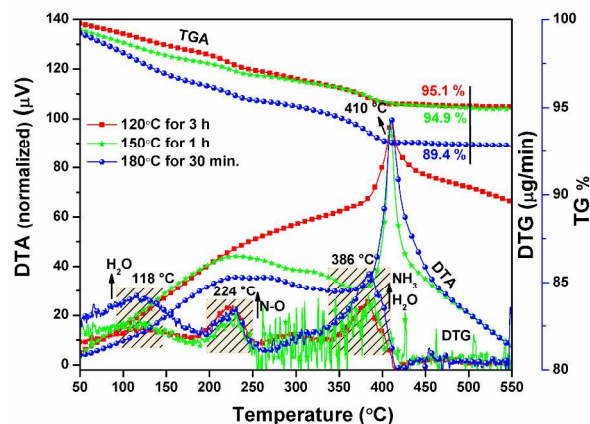


**Fig. 13** TG/DTA/DTG analysis of the as-synthesized  $\text{h-MoO}_3$  synthesized at 120 °C for 3h, 150 °C for 1h and 180 °C for 30 min in the temperature range of 50 °C to 550 °C

In Fig. 13, the TG and DTG curves suggest the presence of three weight losses in the temperature lying between 50 °C and 550 °C. The spectra obtained were identical in nature and showed small deviation in the weight loss percentage (TG - 95.1 % for 120 °C for 3h, 94.9 % for 150 °C for 1h and 89.4 % for 180 °C for 30 min). The first weight loss was observed between 50 °C and 150 °C was attributed to the desorption of physically adsorbed water molecules at the surface of  $\text{h-MoO}_3$  samples. A second weight loss occurred between 200 °C and 250 °C was ascribed to the liberation of volatile by-products associated with the nitrates and ammonium decomposition.

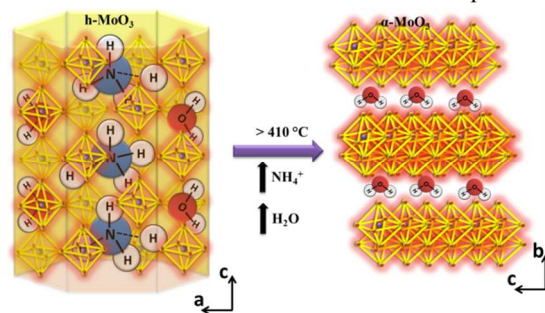


**Fig. 14** Schematic representation of the phase transition behaviour of  $\text{h-MoO}_3$  under heat treatment at 410 °C

The third weight loss with a sharp exothermic peak observed at 410 °C was related to the liberation of  $\text{OH}^-$  and  $\text{NH}_4^+$  ions as  $\text{H}_2\text{O}$  and  $\text{NH}_3$  from the internal structure of  $\text{MoO}_3$ . The removal of  $\text{NH}_3$  (deammoniation) and  $\text{H}_2\text{O}$  (dehydration) from the internal structure of  $\text{h-MoO}_3$  undergoes a mass relocation through dissolution and recrystallization in-situ involve rapid release of the stored chemical potential leads to a change in the

internal energy difference between the hexagonal and orthorhombic phase results in an unstable propagation of phase transition from meta-stable h-MoO<sub>3</sub> to stable α-MoO<sub>3</sub>.<sup>16</sup> The structure of α-MoO<sub>3</sub> thus consist of double layers of zigzag rows of MoO<sub>6</sub> octahedral units which interconnected by covalent forces (corner sharing) along a- and c-axis and the rows mutually connected by van der Waals interactions (edge sharing) along b-axis [001] forms layered architecture as schematically represented in Fig. 14.

### Optical properties

The potential application of the as-obtained h-MoO<sub>3</sub> nanocrystal was considered and the optical characterization of h-MoO<sub>3</sub> with different crystallite sizes and shapes were carried out by measuring DRS. The DRS spectra were recorded in the wavelength ranging from 300 nm to 700 nm (ref. Fig. S10, S11 and Fig. 15). It can be seen that there was a strong reflectance response between 425 nm and 440 nm which indicate the high absorption in the visible region. The strong visible absorption was the characteristic optical absorption of h-MoO<sub>3</sub>. Here, the optical transition is from the vacant “d” orbitals of the cation (Mo<sup>6+</sup>) and “p” orbitals of the oxygen atoms with lone pair of electrons (O<sup>2-</sup>).<sup>27</sup> Fig. S10 presents the variation of reflectance % as a function of wavelength for the samples synthesized under different concentrations of HNO<sub>3</sub> and HCl. The samples synthesized under HNO<sub>3</sub> concentration were defect free and blue shifted. The blue shift in the absorption edge (absorption peak edge towards the lower wavelength region) was assigned to the reduction of the crystallite size of the h-MoO<sub>3</sub> samples. In the case of HCl utilized samples, there was no variation in the absorption edge. However, an asymmetric absorption fall was observed between 550 nm and 700 nm, due to interband transitions originated by the presence of Mo<sup>5+</sup> in h-MoO<sub>3</sub> that act as color centers within the forbidden band. The presence of Mo<sup>5+</sup> was further inferred from the colour perception of h-MoO<sub>3</sub> sample. Here, the sample color (pale yellow for HNO<sub>3</sub>) turned to blue when HCl was used as an oxidant.<sup>28</sup>

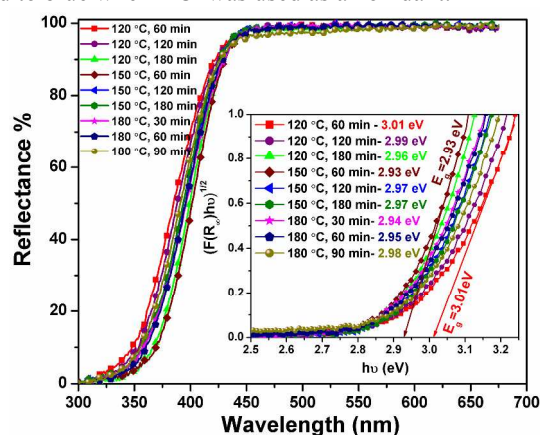


**Fig. 15** UV-Vis diffuse reflectance spectra of as-synthesized h-MoO<sub>3</sub> samples synthesized for different reaction time and temperature; inset shows the band gap of h-MoO<sub>3</sub>

Fig. S11 depicts the DRS spectra of as-synthesized h-MoO<sub>3</sub> samples synthesized under different water, ethanol and heptane used as solvent medium. The defect free band structure was observed and the optical bandgap was estimated from the Kubeka-Munk function<sup>13</sup> and the relation was defined as (ref. Eqn. 1),

$$F(R_{\infty}) = \frac{(1-R_{\infty})^2}{2R_{\infty}} = \frac{K(\lambda)}{s(\lambda)} \propto \alpha = \frac{(h\nu - E_g)^2}{h\nu} \quad (1)$$

where,  $F(R_{\infty})$  is the K-M function or re-emission function,  $R_{\infty}$  is the diffuse reflectance of an infinitely thick sample,  $K(\lambda)$  is the absorption coefficient,  $s(\lambda)$  is the scattering coefficient,  $h\nu$  is the photon energy and  $E_g$  is the bandgap energy for indirect transition, respectively. The bandgap was derived from the plot between the square of the K-M function  $F(R)^2$  and energy. To obtain the optical bandgap, the linear part of  $F(R)^2$  curve was extrapolated and intersected to the energy axis. The estimated optical bandgap values were tabulated in Table 1. The bandgap was found to be 2.95 eV, 2.93 eV and 2.91 eV for water, ethanol and heptane, respectively. This was attributed to the difference in the surface chemistry of particles that affects the bandgap of h-MoO<sub>3</sub>. Fig. 15 present the DRS spectra of samples synthesized under different reaction time and reaction temperature. The optical bandgap can be tuned in the range of 2.93 eV to 3.01 eV. The results suggest that the bandgap difference in h-MoO<sub>3</sub> was dependent on the crystallite size and the defect nature of the samples. Thus, the optical absorption in the visible light regions exhibited by h-MoO<sub>3</sub> proved to be a suitable material for visible light active applications.

### Conclusions

3D hierarchical flower-like microspheres of h-MoO<sub>3</sub> nanocrystals were synthesized by controlling the effective synthesis variables such as chemical oxidant, oxidant concentration, solvent ratio, reaction time and reaction temperature using simple solution based chemical precipitation route. Ultimately, all the reaction variables influence on complex chemical processes and thus making a unique contribution to the formation of uniform and monodispersed single phase h-MoO<sub>3</sub> nanocrystals. From the experimental results, it was found that hierarchical flower-like microspheres are achieved in the presence of HNO<sub>3</sub> of appropriate concentration than using HCl. Among the different solvent medium such as water, ethanol and heptane, the water render uniform dissolution and homogeneity of the reactant molecules for the formation of h-MoO<sub>3</sub>. Further, an appropriate reaction temperature and time provide sufficient energy input to promote the reactants speed and strong attractive interactions resulted controlled nucleation and growth of h-MoO<sub>3</sub>. Based on the results, a well-developed h-MoO<sub>3</sub> nanocrystals was achieved conditions such as HNO<sub>3</sub> of 5 mL concentration, water act as a solvent medium, reaction temperature and time maintained as 120 °C for 180 min, 150 °C for 120 min and 180 °C for 30 h. From the thermal study, it was found that the hexagonal phase stability of the above optimized samples was achieved upto 410 °C and the structure was distinct in comparison to other polymorphs of MoO<sub>3</sub>. The optical absorption exhibited in the visible light region, size dependent bandgap shift and the presence of traps are providing new insights in the materials properties. From the overall investigations, we proposed that the hierarchical flower-like h-MoO<sub>3</sub> nanocrystals is likely to be a model meta-stable materials family for a systematic experimental understanding in the nanomaterial synthesis and used for fabricating advanced functional materials for the industrial applications.

### References

- J. Guan, L. Liu, L. Xu, Z. Sun, and Y. Zhang, *Cryst. Eng. Comm.*, 2011, **13**, 2636-2643.

- 2 V. Polshettiwar, B. Baruwati and R. S. Varma, *ACS Nano*, 2009, **3**, 728-736.
- 3 Z. G. Yan and C. H. Yan, *J. Mater. Chem.*, 2008, **18**, 5046-5059.
- 4 L. Zhang, W. Niu. And G. Xu, *Nano Today*, 2012, **7**, 586-605.
- 5 T. D. Nguyen, C. T. Dinh, and T. O. Do, *Nanoscale*, 2011, **3**, 1861-1873.
- 6 C. N. R. Rao, H. S. S. R. Matte, R. Voggu, and A. Govindaraj, *Dalton Trans.*, 2012, **41**, 5089-5120.
- 7 K. Namratha and K. Byrappa, *Progress in Cryst. Growth Charact. Mater.*, 2012, **58**, 14-42.
- 8 A. L. Tiano, C. Koenigsmann, A. C. Santulli and S. S. Wong, *Chem. Commun.*, 2010, **46**, 8093-8130.
- 9 G. Liu, J. C. Yu, G. Q. Lu and H. M. Cheng, *Chem. Commun.*, 2011, **47**, 6763-6783.
- 10 N. A. Chernova, M. Roppolo, A. C. Dillon and M. S. Whittingham, *J. Mater. Chem.*, 2009, **19**, 2526-2552.
- 11 T. Xia, Q. Li, X. Liu, J. Meng and X. Cao, *J. Phys. Chem. B*, 2006, **110**, 2006-2012.
- 12 A. Chithambararaj and A. C. Bose, *J. Alloys Compd.*, 2011, **509**, 8105-8110.
- 13 A. Chithambararaj and A. C. Bose, *Beilstein J. Nanotechnol.*, 2011, **2**, 585-592.
- 14 L. Zheng, Y. Xu, D. Jin and Y. Xie, *Chem. Mater.*, 2009, **21**, 5681-5690.
- 15 A. Chithambararaj, N. S. Sanjini, A. C. Bose and S. Velmathi, *Catal. Sci. Tech.*, 2013, **3**, 1405-1414.
- 16 A. Chithambararaj, N. S. Sanjini, S. Velmathi and A. C. Bose, *Phys. Chem. Chem. Phys.*, 2013, **15**, 14761-14769.
- 17 R. Yogamalar, R. Srinivasan, A. Vinu, K. Ariga and A. C. Bose, *Solid State Commun.*, 2009, **149**, 1919-1923.
- 18 Y. Muraoka, J. C. Grenier, S. Petit, and M. Pouchard, *Solid State Sci.*, 1999, **1**, 133-148.
- 19 H. I. Chen, and H. Y. Chang, *Colloids Surf. A: Physicochem. Eng. Aspects*, 2004, **242**, 61-69.
- 20 H. Gron, P. Mougín, A. Thomas, G. White, D. Wilkinson, R. B. Hammond, X. Lai, and K. J. Roberts, *Ind. Eng. Chem. Res.*, 2003, **42**, 4888-4898.
- 21 X. Tan, J. Zhou and Q. Yang, *Cryst. Eng. Comm.*, 2011, **13**, 2792-2798.
- 22 L. Xu, X. Yang, Z. Zhai, X. Chao, Z. Zhang and W. Hou, *Cryst. Eng. Comm.*, 2011, **13**, 4921-4929.
- 23 R. Ray and S. Paria, *Ind. Eng. Chem. Res.*, 2011, **50**, 11601-11607.
- 24 R. Marczak, F. Werner, R. Ahmed, V. Lobaz, D. M. Guldi and W. Peukert, *Langmuir*, 2011, **27**, 3920-3929.
- 25 X. Liang, X. Wang, J. Zhuang, Y. Chen, D. Wang and Y. Li, *Adv. Funct. Mater.*, 2006, **16**, 1805-1813.
- 26 H. Gron, P. Mougín, A. Thomas, G. White, D. Wilkinson, R. B. Hammond, X. Lai and K. J. Roberts, *Ind. Eng. Chem. Res.*, 2003, **42**, 4888-4898.
- 27 N. S. P. Bhuvanesh and J. Gopalakrishnan, *J. Mater. Chem.*, 1997, **7**, 2297-2306.
- 28 T. He and J. Yao, *J. Photochem. Photobiol. C: photochem. Rev.*, 2003, **4**, 125-143.

<sup>a</sup> *Nanomaterials Laboratory, Department of Physics, National Institute of Technology, Tiruchirappalli – 620 015, India. E-mail: acbose@nitt.edu*

Electronic Supplementary Information (ESI) available: [S1-S11: S1(a) The peak shift analysis of as-synthesized h-MoO<sub>3</sub> samples prepared with different HNO<sub>3</sub> concentrations; (b) variation of diffraction peak intensity and crystallite size with respect to HNO<sub>3</sub> concentration, S2 The FT-IR spectra of as-synthesized h-MoO<sub>3</sub> samples prepared with different HNO<sub>3</sub> concentrations, S3(a) XRD patterns of as-synthesized h-MoO<sub>3</sub> sample prepared with different HCl concentrations; (b) variation of diffraction peak intensity and crystallite size with respect to HCl concentration, S4 SEM images of as-synthesized h-MoO<sub>3</sub> samples prepared with (a, b) 3 mL; (c, d) 5 mL; (e, f) 10 mL and (g, h) 15 mL HCl concentrations, S5(a) XRD pattern of as-synthesized h-MoO<sub>3</sub> samples synthesized using water/ethanol combination; (b) variation of diffraction peak intensity and crystallite size with respect to ethanol concentration, S6(a) XRD pattern of as-synthesized h-MoO<sub>3</sub> samples synthesized using the water / heptane combination; (b) variation of diffraction peak intensity and crystallite size with respect to heptane concentration, S7 SEM images of as-synthesized h-MoO<sub>3</sub> samples synthesized using water/ethanol compositions, S8 SEM images of as-synthesized h-MoO<sub>3</sub> samples synthesized using water/heptane compositions, S9(a) XRD patterns of h-MoO<sub>3</sub> samples synthesized at different reaction time and reaction temperature; (b) variation of diffraction peak intensity and crystallite size with respect to reaction time and reaction temperature, S10 UV-Vis diffuse reflectance spectra of samples obtained for different HNO<sub>3</sub> and HCl concentrations, S11 UV-Vis diffuse reflectance spectra of as-synthesized h-MoO<sub>3</sub> samples synthesized under water, ethanol and heptane as solvent medium; inset shows the band gap of h-MoO<sub>3</sub>]. See DOI: 10.1039/b000000x/

## Notes

## ARTICLE

## Role of synthesis variables on controlled nucleation and growth of hexagonal molybdenum oxide nanocrystals: Investigation on thermal and optical properties

A. Chithambararaj<sup>a</sup> and A. Chandra Bose<sup>a</sup>

<sup>a</sup> Nanomaterials Laboratory, Department of Physics, National Institute of Technology, Tiruchirappalli – 620 015, India. E-mail: acbose@nitt.edu

**Table 1.** Detailed experimental conditions together with their morphology, crystallite size and band gap of as-synthesized h-MoO<sub>3</sub>

Oxidant	HNO <sub>3</sub> Con. (mL)	Solvent (mL)	Temp. (°C)	Time (min)	Morphology	Crystallite Size (D <sub>210</sub> ) nm	Band Gap (E <sub>g</sub> ) eV
HNO <sub>3</sub>	3	Water (10)	85	60	Distorted hexagonal rods	56	2.95
	5				Flower-like hierarchical microspheres	50	2.99
	10				Non-uniform hexagonal rods	33	3.03
	15				Non-uniform hexagonal rods	29	3.07
HCl	3	Water (10)	120	180	Distorted and non-uniform hexagonal rods	67	2.99
	5				Distorted and non-uniform hexagonal rods	99	3.02
	10				Distorted and non-uniform hexagonal rods	124	3.02
	15				Distorted and non-uniform hexagonal rods	116	3.02
		Water (10)			Flower-like hierarchical microspheres	46	2.95

HNO <sub>3</sub>	5	Ethanol (10)	120	180	Widely distributed hexagonal rods	51	2.93			
		Heptane (10)			Agglomeration and Non-hexagonal rods	24	2.91			
HNO <sub>3</sub>	5	Water (10)	120	60	Distorted hexagonal rods	41	3.01			
				120	Distorted hexagonal rods	48	2.99			
				180	Flower-like hierarchical microspheres	46	2.96			
			150	60	Hierarchical flower-like microspheres	42	2.93			
				120	Rubbed and broken hexagonal rods	41	2.97			
				180	Rubbed and broken hexagonal rods	45	2.97			
			180	30	Flower-like hierarchical microspheres	40	2.94			
				60	Rubbed and broken hexagonal rods	41	2.95			
90	Rubbed and broken hexagonal rods	52		2.98						